Applied Catalysis B: Environmental 309 (2022) 121235

Contents lists available at ScienceDirect

Applied Catalysis B: Environmental

journal homepage: www.elsevier.com/locate/apcatb

# Accelerated iron cycle inducing molecular oxygen activation for deep oxidation of aromatic VOCs in $MoS_2$ co-catalytic $Fe^{3+}$/PMS system

Xiaowen Xie [a], Jiachun Cao [b], Yongjie Xiang [a], Ruijie Xie [a], Ziyi Suo [a], Zhimin Ao [b,*], Xin Yang [a], Haibao Huang [a,*]

[a] School of Environmental Science and Engineering, Sun Yat-Sen University, Guangzhou, China
[b] Institute of Environmental Health and Pollution Control, School of Environmental Science and Engineering, Guangdong University of Technology, Guangzhou, China

ARTICLE INFO

*Keywords:*
Aromatic VOCs
Accelerated iron cycle
Electron transfer
Molecular oxygen activation
Reactive oxygen species

ABSTRACT

In this work, $MoS_2$ is utilized as a cocatalyst to enhance $Fe^{3+}$/PMS reaction for the deep oxidation of aromatic VOCs in a continuous air-bubbling system. The exposed $Mo^{4+}$ active sites achieve high-speed electron transfer from $MoS_2$ (001) surface to $Fe^{3+}$ and accelerate $Fe^{2+}$ regeneration (~60%), which greatly promotes $O_2$ and PMS activation for the formation of radicals like $O_2^{\bullet-}$, $HO^{\bullet}$ and $SO_4^{\bullet-}$. Consequently, the $Fe^{3+}$/PMS/$MoS_2$ system exhibits strong catalytic ability for various VOCs degradation including styrene, toluene and chlorobenzene (with removal efficiency of 97%, 84% and 83%, respectively) at a wide pH range (3−9). $MoS_2$ cocatalyst in $Fe^{3+}$/PMS reaction greatly promotes the activation of $O_2$ into radicals and inhibits the formation of toxic aromatic byproducts via the deep oxidation of styrene into $CO_2$. Our study provides a green strategy to activate $O_2$ for pollutants degradation and has great potential to be widely applied in actual environment remediation.

## 1. Introduction

Volatile organic compounds (VOCs) are regarded as the key precursors to form atmospheric haze and photo-chemical smog [1,2], which cause great harm on human health and environment. Among the anthropogenic VOCs, aromatic hydrocarbons make the greatest contribution to the formation of $O_3$ and secondary organic aerosols (SOAs) due to their massive industrial emission and strong photochemical activity [3,4]. Many aromatic VOCs are highly toxic and malodorous. Therefore, the effective treatment of aromatic VOCs must be emphasized. Catalytic oxidation technology, such as photocatalysis, ozone catalytic oxidation, catalytic combustion, has been widely used in VOCs waste gas treatment [5,6]. However, the application of these methods in industrial process is greatly limited by disadvantages such as the catalyst poisoning, high energy consumption, complicated operation and secondary air-pollution [7,8]. These weaknesses greatly limit its application in industries.

Recently, advanced oxidation processes (AOPs) have attracted much interest in VOCs degradation via a wet bubbling reactor [9–11]. Due to the generation of strong reactive oxygen species (ROS) like hydroxyl radical ($HO^{\bullet}$), sulfate radical ($SO_4^{\bullet-}$), VOCs could be degraded into small molecules and even mineralized into $CO_2$ and $H_2O$, which could efficiently avoid the secondary air-pollution in the traditional heterogeneous catalysis (gas-solid) methods [12]. An efficient mass transfer of the contaminants from the gas to the liquid can be achieved by the occurrence of such chemical reaction [9]. Furthermore, the VOCs waste gas containing $O_2$ is continuously fed into the reactor to proceed the oxidation reaction [9,13]. As is known, $O_2$ is the greenest and most economical oxidant in environment. Efficient activation of $O_2$ is crucial for catalytic degradation of pollutants [14]. However, conventional catalytic oxidation technologies require harsh reaction conditions and high energy consumption to activate $O_2$. In our previous study [15], it was proposed that UV/PDS coupled with wet-bubbling process can achieve the efficient degradation and mineralization of gaseous chlorobenzene in the presence of $O_2$. But a large number of high toxic byproducts were generated without $O_2$, indicating that $O_2$ played an important role in chlorobenzene oxidation. Though the activation method via UV was quite efficient, it led to high cost and energy consumption. It is still a big challenge to activate $O_2$ in mild conditions for VOCs degradation. As reported, $O_2$ can accept electron from $Fe^{2+}$ to produce various ROS in Fenton reaction, including $O_2^{\bullet-}$, $HO^{\bullet}$ and $H_2O_2$ (Eqs. 1–4), which can promote the degradation of pollutants [16,17].

$$Fe^{2+} + O_2 \rightarrow Fe^{3+} + O_2^{\bullet-} \quad (1)$$

$$Fe^{2+} + O_2^{\bullet-} + 2\,H^{+} \rightarrow Fe^{+} + H_2O_2 \quad (2)$$

* Corresponding authors.
*E-mail addresses:* zhimin.ao@gdut.edu.cn (Z. Ao), huanghb6@sysu.edu.cn (H. Huang).

https://doi.org/10.1016/j.apcatb.2022.121235
Received 6 November 2021; Received in revised form 17 February 2022; Accepted 20 February 2022
Available online 23 February 2022

$$2\ O_2^{\bullet-} + 2\ H^+ \rightarrow H_2O_2 + O_2 \quad (3)$$

$$Fe^{2+} + H_2O_2 \rightarrow Fe^{3+} + HO^{\bullet} + HO^- \quad (4)$$

However, the slow reduction rate of $Fe^{3+}$ to $Fe^{2+}$ in Fenton process greatly limits its practical application in industries. Actually, the essence of $Fe^{3+}$ reduction is to accept extra electrons. High-speed electron transfer has an important impact on improving the efficiency of Fenton reaction [18]. Some works utilized organic reducing agents like hydroxylamine, ascorbic acid, protocatechuic acid, cysteine as co-catalyst to prevent iron precipitation and accelerate the $Fe^{3+}/Fe^{2+}$ conversion in Fenton reaction [19–21]. But unfortunately, the organic compounds as the co-catalysts easily caused secondary pollution due to the uncompleted mineralization of pollutants and organic co-catalysts, and was greatly limited by its poor cycling stability. Xing et al. [22] proposed that $MoS_2$ can serve as an excellent co-catalyst to accelerate the $Fe^{3+}/Fe^{2+}$ cycle in $Fe^{2+}/H_2O_2$ system due to the exposed reductive metallic active sites, which greatly increased the decomposition efficiency of $H_2O_2$ and decreased the consumption of $H_2O_2$ and $Fe^{2+}$. Furthermore, $MoS_2$ can achieve 90% total organic carbon (TOC) degradation rate even after repeated reactions for ten cycles, which proved its great reusability and stability. However, they also found that the degradation performance of pollutants was not significantly affected by $O_2$. If $O_2$ can be activated to promote ROS generation in Fenton reaction, the better degradation performances of target pollutants may be obtained with less oxidant ($H_2O_2$, PMS, etc.) and cost. Therefore, it is highly necessary to boost $O_2$ activation and clarify its mechanism for catalytic degradation of pollutants.

$MoS_2$ possesses remarkable reduction ability to reduce $Fe^{3+}$ and maintain iron in soluble forms and also accelerate the $Fe^{3+}/Fe^{2+}$ cycle for the efficient Fenton oxidation. Compared with the instability of $Fe^{2+}$, $Fe^{3+}$ are ubiquitous in natural water environments in spite of tiny amount [23]. Xing et al. [24] proved that the pollutants degradation performance in $Fe^{3+}$/PMS system were substantially the same as that in the $Fe^{2+}$/PMS system when adding $MoO_2$ as the co-catalyst. Zhang et al. [23] also proposed that the presence of protocatechuic acid (PCA) guaranteed the sufficient supply of $Fe^{2+}$ in both the $Fe^{2+}$/PCA/$H_2O_2$ and $Fe^{3+}$/PCA/$H_2O_2$ systems, accounting for the similar alachlor degradation performances. Thus, $Fe^{3+}$ as a catalyst is more realistic in natural aquatic environments via Fenton oxidation processes. In this study, we realized the efficient activation of molecular $O_2$ via the accelerated $Fe^{2+}$ regeneration through the co-catalytic effect of $MoS_2$ in the air-bubbling Fenton reaction. The $Fe^{3+}$/PMS/$MoS_2$ system achieved an efficient and continuous degradation of various VOCs (including styrene, toluene and chlorobenzene) at a wide pH range (3−9). Density functional theory (DFT) calculations and experiments proved that $Fe^{3+}$ ions can be adsorbed around the sulfur vacancies on $MoS_2$ (001) surface to achieve continuous high-speed electron transfer for efficient activation of PMS and $O_2$. The intermediates detected by PTR-ToF-MS showed that the presence of $O_2$ can greatly reduce the generation of toxic byproducts. This work utilized $MoS_2$ as a cocatalyst to accelerate the $Fe^{2+}$ regeneration in $Fe^{3+}$/PMS reaction for the deep oxidation of VOCs via the efficient activation of $O_2$ and PMS, which is expected to greatly promote advances in practical applications of industrial waste gas treatment.

## 2. Materials and methods

### 2.1. Equipment and procedures

The degradation of VOCs in $Fe^{3+}$/PMS/$MoS_2$ system was conducted in a micro-bubbling reactor, which depended on the feeding of a gaseous stream in the bottom of the column through a gas disperser [11]. The reactor with an effective working volume of 1 L was consisted of gas distribution system, reaction system and analytic system (Fig. S1). The air was fed through the bottom of the reactor by an air pump, and a mass flowmeter was used to control the flow rate of supplied air (1 L $min^{-1}$). Styrene, a typical odor aromatic VOCs, was selected as the model pollutants to study its degradation performances and mechanisms. The experiments were initiated by the addition of $MoS_2$, $Fe^{3+}$ and PMS to the solution. To clarify the role of molecular $O_2$ on styrene degradation, high-purity $N_2$ was bubbled into the solution for 30 min before reaction and during the entire degradation process to remove molecular oxygen.

### 2.2. Analytical methods

A gas chromatograph (GC) (9790II, Fuli) equipped with two flame-ionization detectors (FID) was applied to measure the inlet and outlet concentrations of styrene and $CO_2$ on line. The column temperature, injector temperature and detector temperature of GC were set as 70 ℃, 200 ℃ and 250 ℃, respectively. The PMS concentration was detected by the improved iodimetry titration method [25,26]. 100 μL sample solution was dissolved in 50.0 mL KI (0.60 M) and $NaHCO_3$ (0.48 M) mixed solution, then shaking and dispersing the solution to balance it for 15 min before detection by a UV–vis spectrophotometer (Shimadzu, UV2550) at 352 nm. The concentrations of Mo ions in solution were measured by ICP-OES spectrometer (Perkin Elmer, Optima 5300DV). A proton transfer reaction-time of flight-mass spectrometer (PTR-ToF-MS, Ionicon Analytik GmbH, Innsbruck, Australia) was used to detected the produced intermediates. Electron paramagnetic resonance (EPR) test was applied to testify the existence of radicals with DMPO and TEMP as the spin trapping reagent. The detail procedures can be found in the Supporting information. The quality active analysis of $HO^{\bullet}$ was used by the coumarin photoluminescence (PL) technique. The concentration of dissolved $Fe^{2+}$ and $Fe^{3+}$ ion was quantified by the colorimetric method, which was described in detail in Supporting information.

The removal efficiency of styrene was calculated by equations as follows:

$$\text{Removal efficiency} = \frac{[\text{Styrene}]_{\text{inlet}} - [\text{Styrene}]_{\text{outlet}}}{[\text{Styrene}]_{\text{inlet}}} \times 100\%$$

where $[\text{Styrene}]_{\text{inlet}}$ and $[\text{Styrene}]_{\text{outlet}}$ represented the concentrations of gas styrene at the inlet and outlet, ppmv.

### 2.3. DFT theoretical methodology

The spin-unrestricted density functional theory (DFT) calculations were performed by using $Dmol^3$ package [27]. Generalized gradient approximation (GGA) with Perdew-Burke-Ernzerhof (PBE) method was used as the exchange-correlation function [28]. The relativistic effects were treated by DFT semicore pseudopotentials (DSPPs), and the core electrons were replaced by a single effective potential. Double numerical plus polarization (DNP) was used as the basis set. The convergence tolerance of energy of $10^{-5}$ hartree was taken (1 hartree = 27.21 eV), and the maximal allowed force and displacement were 0.002 hartree per Å and 0.005 Å, respectively. In the simulation process, three-dimensional periodic boundary conditions were taken. The simulation cell consists of a 4 × 4 supercell of $MoS_2$ (001) with a vacuum width of 15 Å above the substrate layer to minimize the interlayer interaction. A (3 × 3 × 1) Monkhorst-Pack mesh was used for the Brillouin-zone. The DFT+D method within the TS scheme was used in all calculations to consider the van der Waals forces [29] and the COSMO method was implied to consider the solution environment [30]. The amount of charge transfer (Mulliken charge) between the adsorbed PMS molecule and $MoS_2$ surface was also analyzed to reveal the activation mechanism.

The interaction between adsorbates and $MoS_2$ (001) surface can be evaluated by the adsorption energy ($E_{ads}$), which can be defined by:

$$E_{ads} = E_{total} - E_{sur} - E_{mole/Fe}$$

where $E_{total}$ was the total energy for the adsorption state, $E_{sur}$ was the energy of pure surface, and $E_{mole/Fe}$ was the energy of the adsorbed

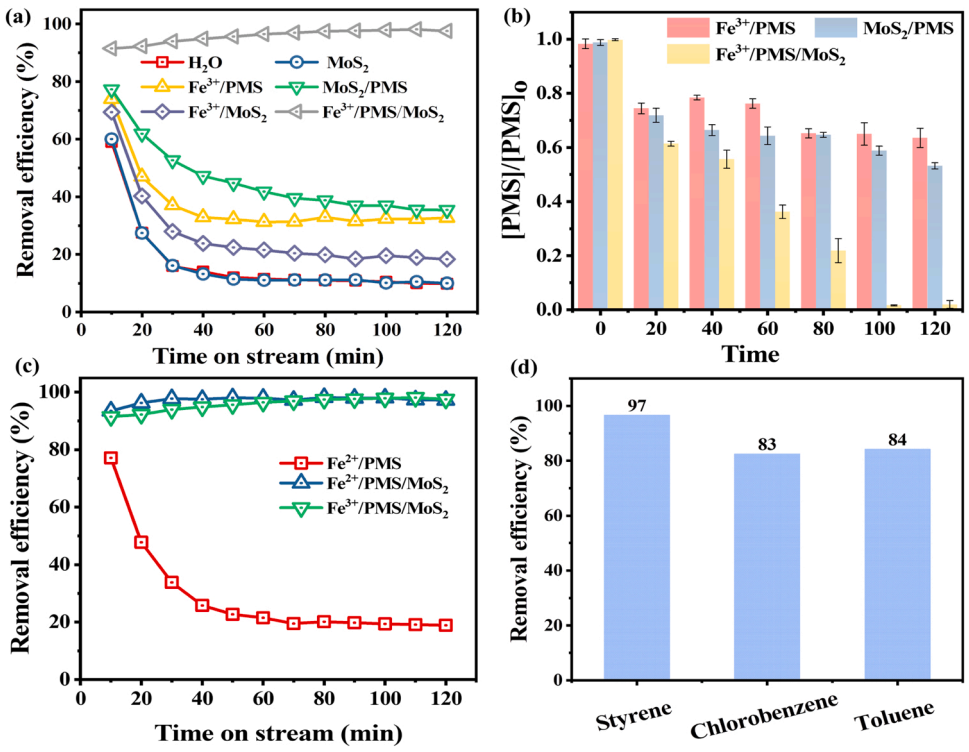


**Fig. 1.** The removal efficiency of styrene (a) and percentage of remaining PMS (b) in different system; Removal efficiency of styrene in different Fenton-like system (c); The degradation performances of $Fe^{3+}$/PMS/$MoS_2$ system to different aromatic VOCs (d). ($[Styrene]_o$ =30 ppmv, $[Fe^{3+}]_o$ = 0.50 mM, $[Fe^{2+}]_o$ = 0.50 mM, $[MoS_2]_o$ = 15 mg, $[PMS]_o$ = 1.6 mM, $pH_o$ = 7, T = 25 ℃).

molecule or Fe atom.

The detailed information of chemical reagents and characterization methods are given in the Supporting information.

## 3. Results and discussion

### 3.1. VOCs degradation in $Fe^{3+}$/PMS/$MoS_2$ system

Herein, $MoS_2$ co-catalytic $Fe^{3+}$/PMS was first used to degrade gaseous styrene in air-bubbling reactor. To begin with, the influence of various factors on styrene removal was systematically studied, including initial $pH_o$, $Fe^{3+}$, $MoS_2$ and PMS dose, gas flow rate (Figs. S2–4). The optimal operating reaction under the conditions of 30 ppmv styrene at air velocity of 1 L $min^{-1}$ was as follows: the $pH_o$ value, the dose of $Fe^{3+}$, $MoS_2$ and PMS were 7, 0.5 mM, 15 mg and 1.6 mM, respectively. As seen in Fig. 1a, styrene removal efficiency decreased quickly from 60% to 10% in the initial 20 min in the case of $H_2O$ absorption. The decreased styrene removal efficiency was attributed to its hydrophobic property and accumulation in water, which suppressed the mass transferring force [31,32]. The similar styrene removal efficiency in pure $H_2O$ and $MoS_2$ solution indicated the poor adsorption of $MoS_2$ to styrene. A mixture of $Fe^{3+}$/$MoS_2$ cannot oxidize styrene in the absence of PMS. Interestingly, the removal efficiency of styrene was up to 98% in $Fe^{3+}$/PMS/$MoS_2$ system and PMS was almost completely consumed after reaction (Fig. 1b). However, the styrene removal efficiency in $Fe^{3+}$/PMS (33%) and $MoS_2$/PMS (35%) system was far lower than that in $Fe^{3+}$/PMS/$MoS_2$, and the remaining PMS in solution was 63% and 53%, respectively. This suggested that $MoS_2$ was highly efficient to promote styrene degradation in Fenton reaction, which was possibly ascribed to the efficient activation of PMS by the accelerated $Fe^{3+}$/$Fe^{2+}$ cycle. After stopping styrene bubbling and re-adding PMS into the solution, the removal efficiency of styrene reached 100%, the outlet $CO_2$ concentration rose to 275 ppmv and then decreased to almost zero (Fig. S5). No excessive by-products were detected in both outlet gas and solution (Fig. S6), indicating that the residual styrene and accumulated intermediates were completely degraded and mineralized into $CO_2$ and $H_2O$. This greatly avoided the environmental risk from the emission of toxic styrene and its byproducts.

It is well known that the bottleneck of Fenton reaction is the slow $Fe^{3+}$/$Fe^{2+}$ cycle [33–35]. To clarify the role of $MoS_2$ in Fenton reaction, the styrene degradation in $Fe^{2+}$/PMS system with/without $MoS_2$ was conducted. In Fig. 1c, the styrene removal efficiency decreased rapidly from 77% to 19% in $Fe^{2+}$/PMS system, suggesting the termination of reactions because of the rapid exhaustion and slow regeneration of $Fe^{2+}$ [36]. Interestingly, the $Fe^{2+}$/PMS/$MoS_2$ system showed a similar degradation performance to styrene compared with $Fe^{3+}$/PMS/$MoS_2$, indicating that the styrene degradation was not affected whether $Fe^{2+}$ or $Fe^{3+}$ was used as the catalyst. This was perhaps because $MoS_2$ promoted the efficient $Fe^{3+}$/$Fe^{2+}$ cycle in Fenton reaction [24,36]. Besides styrene, $MoS_2$ can also assist $Fe^{3+}$/PMS to degrade toluene and chlorobenzene (Fig. 1d), suggesting its broad applicability for aromatic VOCs degradation. To prove the stability of $MoS_2$ in $Fe^{3+}$/PMS system, the leaching of Mo ions in reaction solution was detected by ICP-OES. As Fig. 2a showed, the Mo ions concentration after reaction was approximately 1.2 mg $L^{-1}$, accounting for 4% of the total Mo in added $MoS_2$. However, the removal rate of styrene still maintained above 80% after four successive adding PMS and stable for 960 min (Fig. 2b). The XRD, SEM and TEM (Fig. 2c-g) results illustrated no obvious change in crystallinity and morphology of $MoS_2$ before and after the reaction. The above results indicated that $MoS_2$ equipped with the strong structural stability and possibility of practical application in Fenton system. Therefore, it was concluded that the air-bubbling $Fe^{3+}$/PMS/$MoS_2$ system was extensive in the treatment of various VOCs and able to achieve their completed mineralization without any byproducts generation.

### 3.2. Identification of reactive oxygen species

According to the above analysis, it was known that $MoS_2$ as a

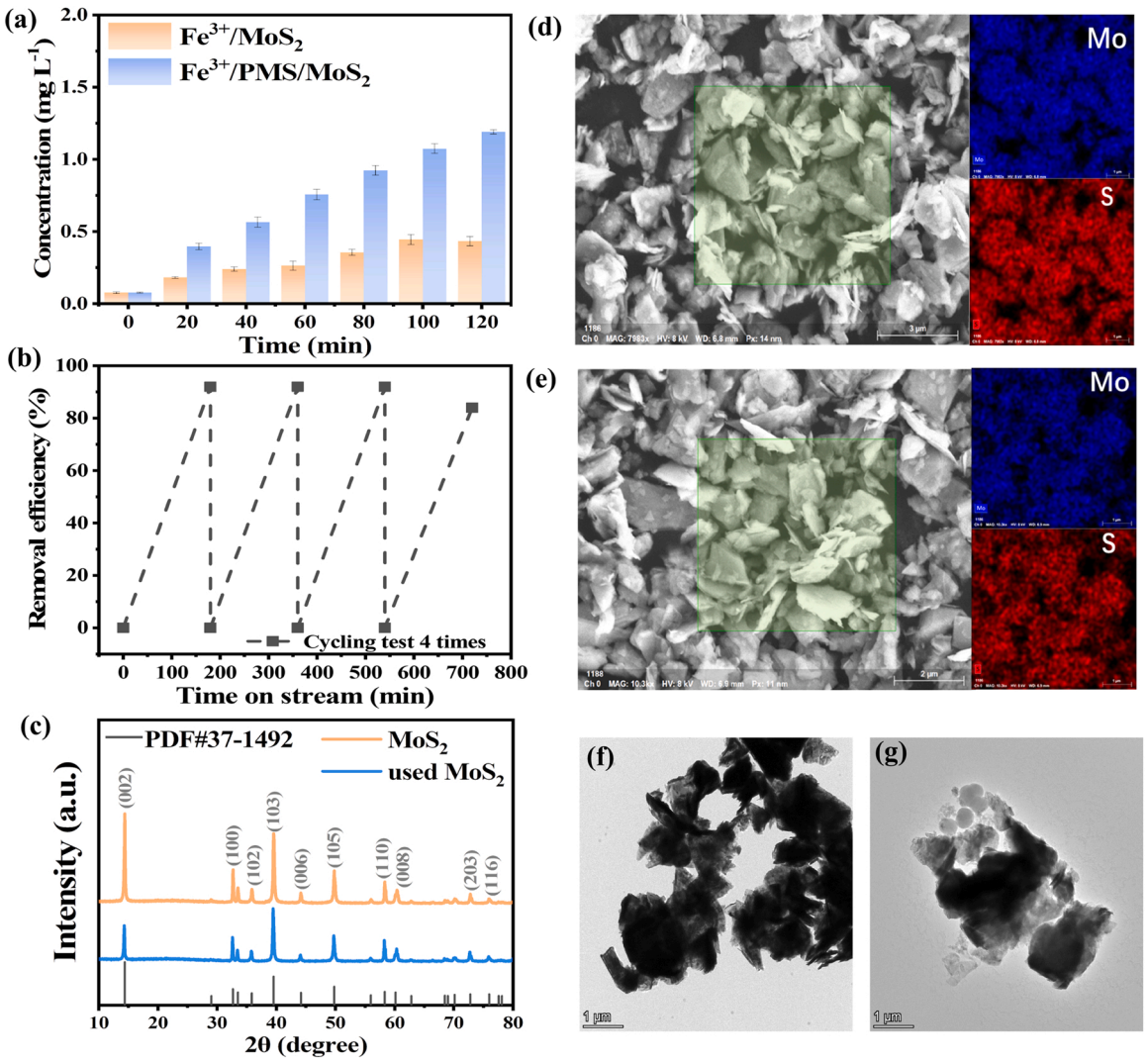


**Fig. 2.** The leaching concentration of molybdenum ions in different reaction system (a); Cycling test of $MoS_2$ co-catalytic $Fe^{3+}$/PMS system by re-adding PMS (b); XRD patterns (c), SEM and EDS mapping images (d and e), TEM images (f and g) of $MoS_2$ before and after reaction.

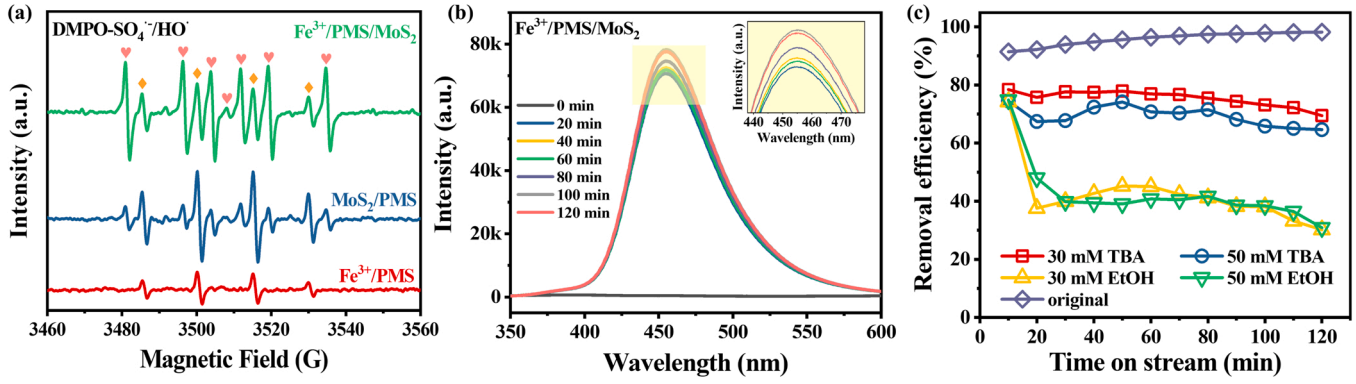


**Fig. 3.** EPR spectra of $HO^{\bullet}$ and $SO_4^{\bullet-}$ produced in $Fe^{3+}$/PMS, $MoS_2$/PMS and $MoS_2$ co-catalytic $Fe^{3+}$/PMS system, with DMPO as trapping agent (a); PL intensity of 7-hydroxycoumarin in $Fe^{3+}$/PMS/$MoS_2$ system under air-bubbling condition (b); Effect of quenching agents on styrene degradation (c). ($[Styrene]_o$ =30 ppmv, $[Fe^{3+}]_o$ = 0.50 mM, $[MoS_2]_o$ = 15 mg, $[PMS]_o$ = 1.6 mM, $pH_o$ = 7, T = 25 ℃; $[Coumarin]_o$ = 1 mM; $[TBA]_o$ = 30, 50 mM, $[EtOH]_o$ = 30, 50 mM; ♦: DMPO-$HO^{\bullet}$, ♥: DMPO-$SO_4^{\bullet-}$).

cocatalyst greatly promoted the oxidation activity of Fenton reaction, but the oxidation mechanism was still unclear. Herein, EPR tests with DMPO as spin trap agent were first performed to identify the ROS in system. In Fig. 3a, only a weak signal of $HO^{\bullet}$ and no obvious signal of $SO_4^{\bullet-}$ was observed in $Fe^{3+}$/PMS system [20]. Surprisingly, both $HO^{\bullet}$ and $SO_4^{\bullet-}$ were observed in $MoS_2$/PMS and $Fe^{3+}$/PMS/$MoS_2$ systems.

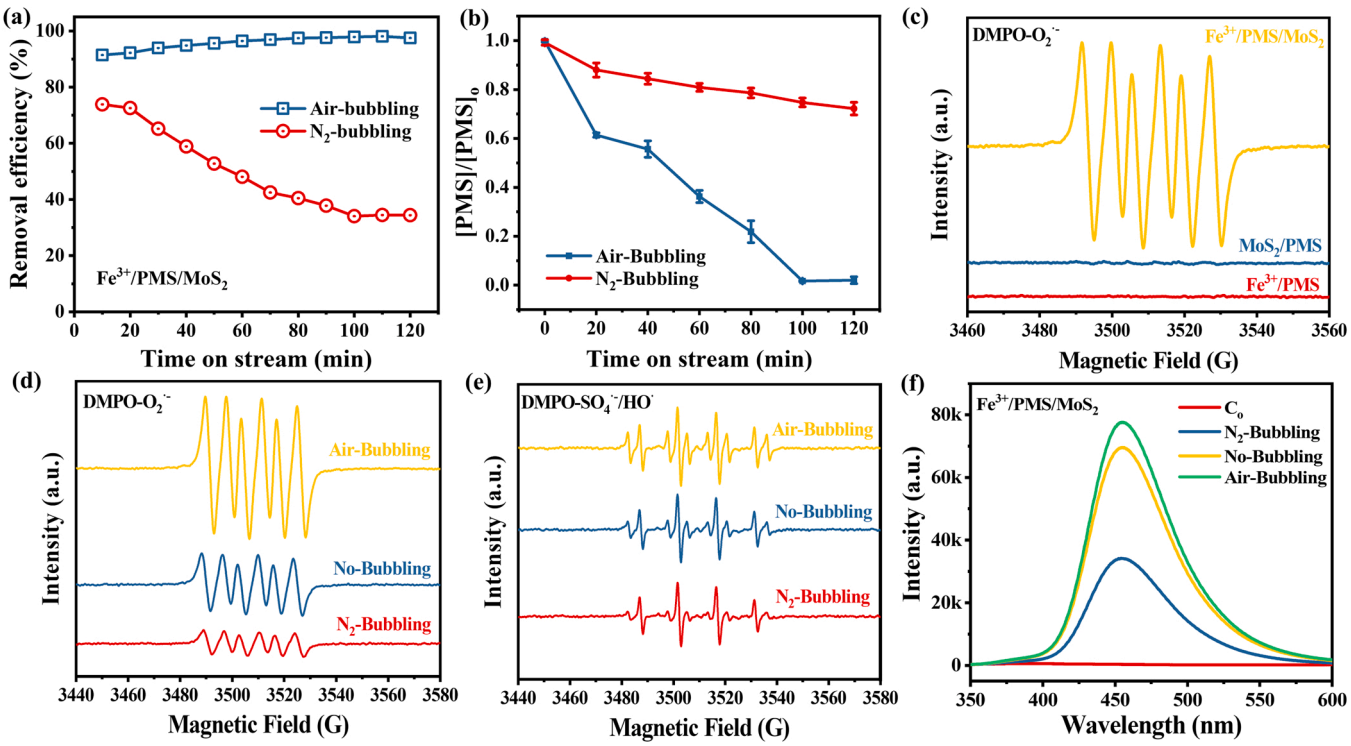


**Fig. 4.** The removal efficiency of styrene (a) and percentage of remaining PMS (b) under different conditions in $Fe^{3+}$/PMS/$MoS_2$ system; The $O_2^{\bullet-}$ signal under air-bubbling condition in different reaction systems (c); The $O_2^{\bullet-}$ (d), $HO^{\bullet}$ and $SO_4^{\bullet-}$ (e) signal, PL intensity of 7-hydroxycoumarin (f) under different conditions in $Fe^{3+}$/PMS/$MoS_2$ system. ([Styrene]$_o$ =30 ppmv, [$Fe^{3+}$]$_o$ = 0.50 mM, [$MoS_2$]$_o$ = 15 mg, [PMS]$_o$ = 1.6 mM, pH$_o$ = 7, T = 25 ℃, [Coumarin]$_o$ = 1 mM).

But the latter showed an obvious increase of $SO_4^{\bullet-}$ compared with the former. In Fig. 3b, the intensity of coumarin PL gradually increased over time, indicating that more and more $HO^{\bullet}$ was produced. Sacrificial experiments were further conducted to make clear the contribution of $HO^{\bullet}$ and $SO_4^{\bullet-}$ in $Fe^{3+}$/PMS/$MoS_2$ system. According to the difference of rate constant between quenching agents and ROS, EtOH was used as a probe of both $SO_4^{\bullet-}$ and $HO^{\bullet}$ ($k_2$(EtOH, $HO^{\bullet}$) = 1.6–7.7 × $10^9$, $k_2$(EtOH, $SO_4^{\bullet-}$) = 1.2–2.8 × $10^7$ $M^{-1}$ $s^{-1}$), while TBA as a probe of only $HO^{\bullet}$ ($k_2$(TBA, $HO^{\bullet}$) = 3.8–7.6 × $10^8$ $M^{-1}$ $s^{-1}$, $k_2$(TBA, $SO_4^{\bullet-}$) = 4.0–9.1 × $10^5$ $M^{-1}$ $s^{-1}$) [37,38]. The styrene removal efficiency decreased from 98% to 69% and 30% with the addition of 30 mM TBA and EtOH, respectively (Fig. 3c). Further increasing their concentration to 50 mM did not significantly affect the degradation of styrene. This suggested that both of them inhibited styrene degradation, and EtOH had a relatively higher inhibitory effect. However, the adsorption of styrene in pure $H_2O$ was just 10%. Here, the styrene removal efficiency dropped to 30% when $SO_4^{\bullet-}$ and $HO^{\bullet}$ were simultaneously quenched, indicating that other oxygen species, such as $O_2$, may be involved in the oxidation process of styrene.

Therefore, the experiments under $N_2$-bubbling condition were conducted to clarify the contribution of $O_2$ on styrene degradation. As seen in Fig. 4a and b, the styrene removal efficiency was markedly reduced from 96% to 35% and the residual PMS maintained above 75% with bubbling $N_2$. The activation of PMS was greatly inhibited in the absence of $O_2$. Figs. S7–8 proved that the molecular $O_2$ in the gas stream participated in the degradation of styrene via increasing the dissolved oxygen concentration in solution. It is well known that $O_2$ can accept electron from $Fe^{2+}$ to produce $O_2^{\bullet-}$, which is a common ROS in AOPs [17,39]. Superoxide dismutase (SOD) as the scavenger of $O_2^{\bullet-}$ was employed to verify its inhibitory effect on styrene degradation. As seen in the revised Fig. S9, the removal efficiency of styrene decreased with the increase of SOD concentration. When the SOD concentration increased from 15 to 30 U $mL^{-1}$, the styrene removal efficiency decreased from 34% to 17%. Further increasing the SOD concentration to 50 U $mL^{-1}$ had no significant effect on styrene removal efficiency, indicating that the styrene degradation has been completely inhibited. This demonstrated that the presence of SOD markedly inhibited the generation of radical species including $O_2^{\bullet-}$, $HO^{\bullet}$ and $SO_4^{\bullet-}$. Fig. 3c shows that the styrene removal efficiency was 30% upon the addition of EtOH. Herein, the inhibition effect of SOD on styrene degradation was much higher than that of EtOH, demonstrating that $O_2^{\bullet-}$ did participate in the degradation of styrene. The EPR signal of $O_2^{\bullet-}$ in $Fe^{3+}$/PMS/$MoS_2$ system was much stronger than that in $Fe^{3+}$/PMS and $MoS_2$/PMS (Fig. 4c), indicating that the addition of $MoS_2$ significantly promoted the formation of $O_2^{\bullet-}$. However, the $O_2^{\bullet-}$ signal was obviously suppressed under no/$N_2$ bubbling condition (Fig. 4d), and the $SO_4^{\bullet-}$ and $HO^{\bullet}$ signal intensities under different conditions were highly positively correlated with that of $O_2^{\bullet-}$ (Fig. 4e and f). This confirmed that the produced $O_2^{\bullet-}$ from $O_2$ activation promoted the generation of $HO^{\bullet}$ and $SO_4^{\bullet-}$ [40,41]. Additionally, the PL intensity of $HO^{\bullet}$ decreased gradually with time under no/$N_2$ bubbling condition (Fig. S10), which may be due to the partial transformation of $HO^{\bullet}$ to $^1O_2$ [40,42]. $^1O_2$ is the lowest and most stable excited state of molecular oxygen and is a highly selective reactive species [42], which reacts almost exclusively with unsaturated organics via electrophilic addition and electron abstraction [43]. However, the second order rate constants between $^1O_2$ and VOCs ($10^0$ to $10^2$ $M^{-1}$ $s^{-1}$) is much lower than that between $O_4^{\bullet-}$/$HO^{\bullet}$ and VOCs ($10^8$ to $10^{10}$ $M^{-1}$ $s^{-1}$) [44]. Fig. S11 showed that the removal efficiency of styrene decreased from 98% to nearly 90% upon the addition of TEMP, indicating that the effect of $^1O_2$ on styrene degradation was slight and even negligible. In Fig. S12, the $^1O_2$ signal air-bubbling condition under air-bubbling condition was much weaker than that under no/$N_2$--bubbling condition, which may be explained by the inhibited transformation of $O_2^{\bullet-}$ to $^1O_2$ due to the strong intensity of $HO^{\bullet}$ and $SO_4^{\bullet-}$ under air-bubbling condition [40]. As reported, the strong $HO^{\bullet}$ (1.9–2.7 V) and $SO_4^{\bullet-}$ (2.5–3.1 V) would mask the oxidation performance of $O_2^{\bullet-}$ (2.4 V) in the conversion to $^1O_2$ (2.2 V) [45,46]. $^1O_2$ has little effect on styrene degradation, while $O_2^{\bullet-}$ makes inhibitory effect. It

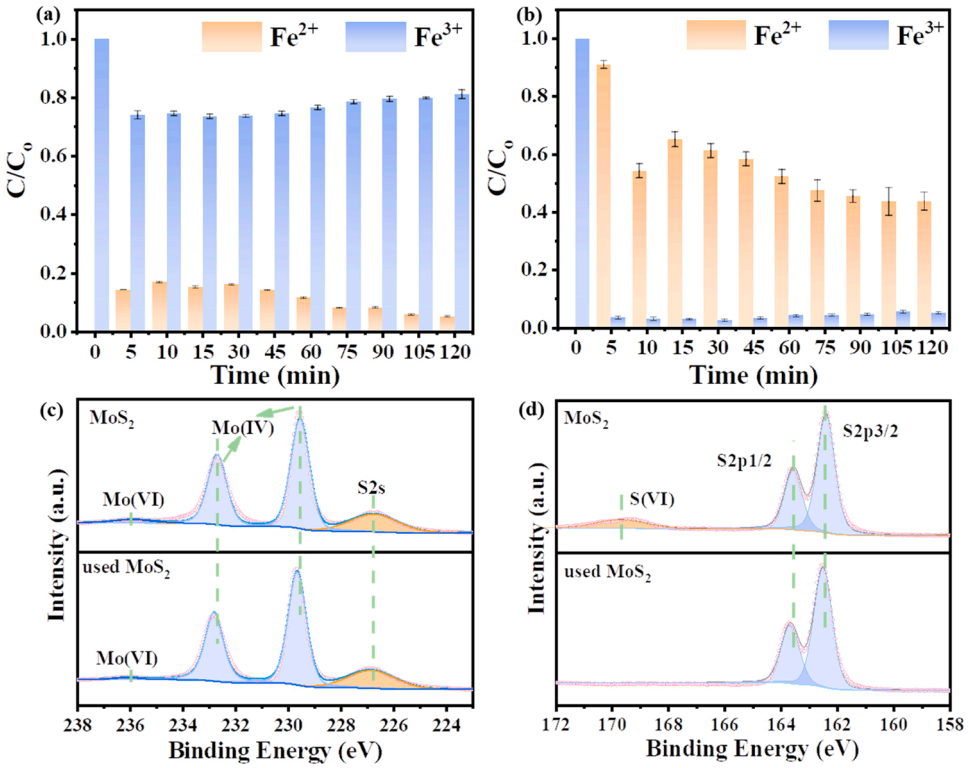


**Fig. 5.** The variation of $Fe^{2+}$ and $Fe^{3+}$ concentration in solution without (a) and with (b) the addition of $MoS_2$, with 1,10-phenanthroline (1 mg $mL^{-1}$) and potassium thiocyanate (KSCN, 10 mg $mL^{-1}$) as the chromogenic reagents; XPS spectrums of $MoS_2$ before and after reaction for Mo3d (c) and S2p (d). ($[Fe^{3+}]_o$ = 0.50 mM, $[MoS_2]_o$ = 15 mg, $[PMS]_o$ = 1.6 mM, $pH_o$ = 7, T = 25 ℃).

is thus reasonable to infer that $O_2^{\bullet-}$ was directly involved in the degradation of styrene instead of transforming into of $^1O_2$. Similar to the degradation of styrene, $O_2$ also had a certain impact on the degradation of chlorobenzene and toluene (Fig. S13), which further indicated that $O_2$ did play an important role in the degradation of aromatic VOCs.

In summary, we concluded that the enhanced $O_2^{\bullet-}$ originating from $O_2$ activation as well as $HO^{\bullet}$ and $SO_4^{\bullet-}$ acted together on styrene degradation in $Fe^{3+}$/PMS/$MoS_2$ system.

### 3.3. Iron cycle mechanism

The previous results showed that $O_2^{\bullet-}$ from $O_2$ significantly promoted the generation of $HO^{\bullet}$ and $SO_4^{\bullet-}$, which may be attributed to the accelerated $Fe^{3+}/Fe^{2+}$ cycle [16,47,48]. To better understand the activation mechanism of PMS and $O_2$ in $Fe^{3+}$/PMS/$MoS_2$ system, the conversion of $Fe^{2+}/Fe^{3+}$ was studied. 1,10-phenanthroline and KSCN were selected as the developer for $Fe^{2+}$ and $Fe^{3+}$, respectively. In $Fe^{3+}$/PMS

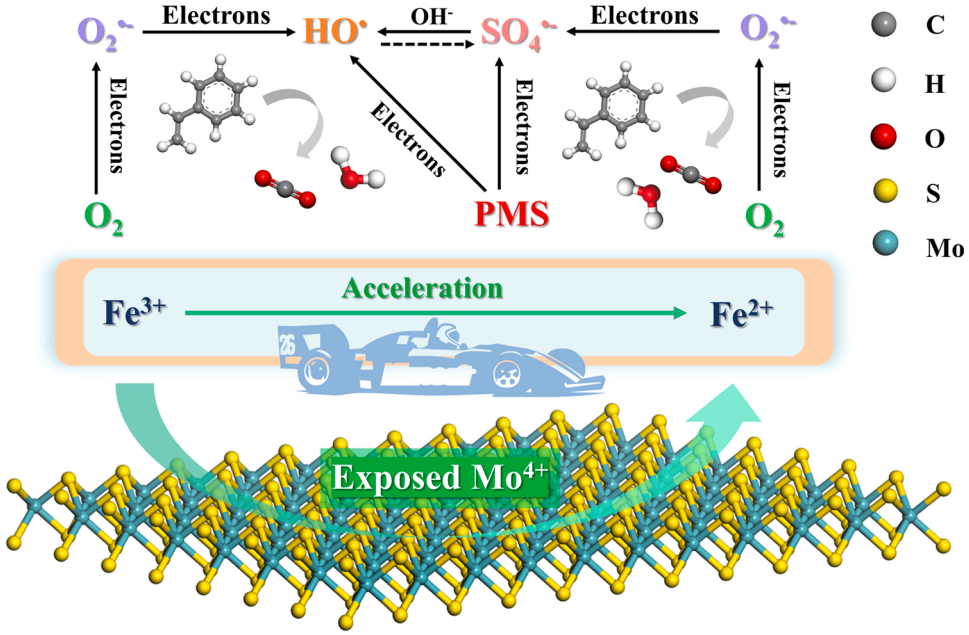


**Fig. 6.** Illustration of the accelerated iron cycle inducing PMS and $O_2$ activation for styrene degradation in $Fe^{3+}$/PMS/$MoS_2$ system.

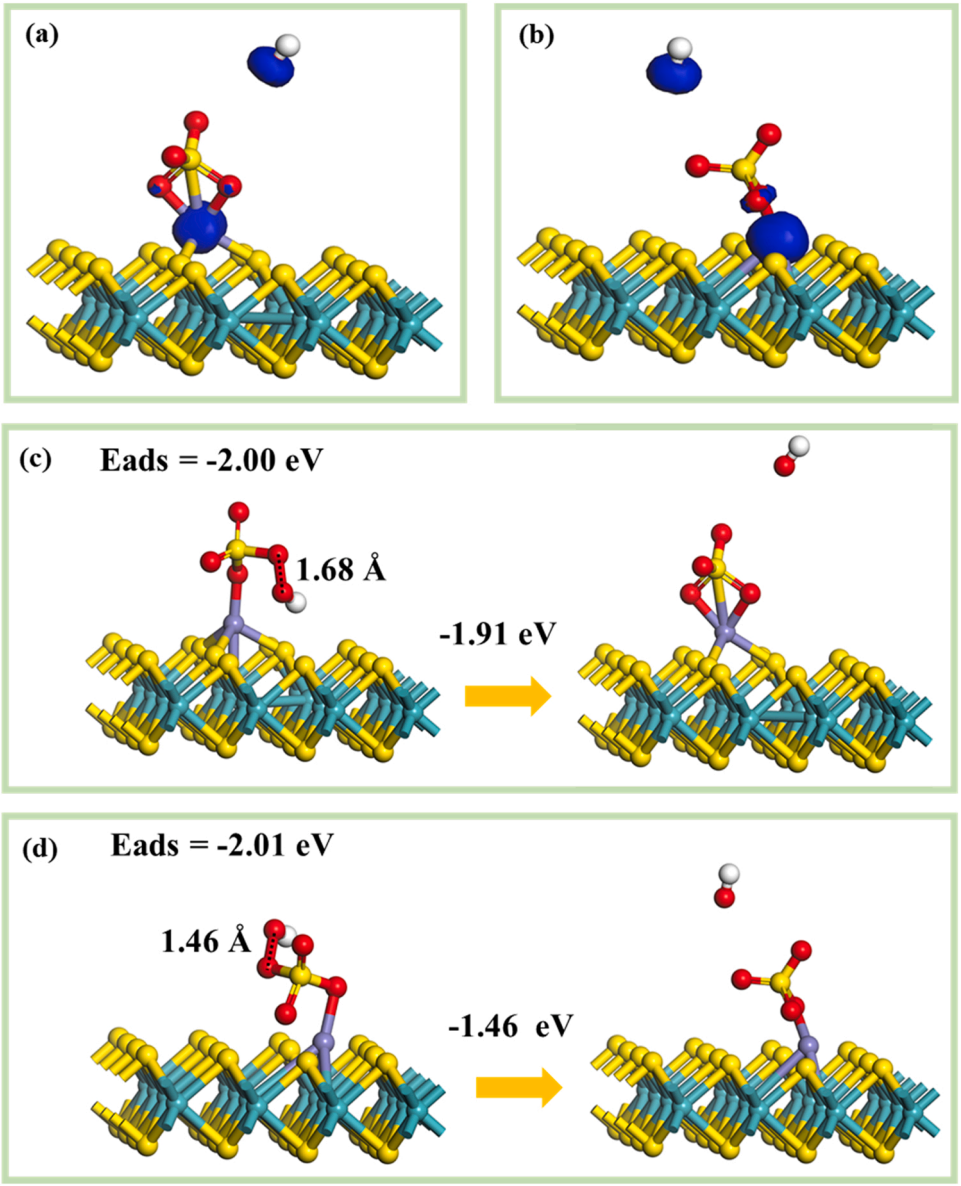


**Fig. 7.** The spin density of product structures of PMS dissociation on the (001)-Fe-Vs (a) and (001)-Fe-G (b) surfaces; The activation process of PMS on $MoS_2$ (001) surface: the adsorption and $HO^{\bullet}$ generation process of $HSO_5^-$ on (001)-Fe-G surface (c) and (001)-Fe-Vs surface (d). The indigo, yellow, purple, red and white balls represent Mo, S, Fe, O and H atoms, respectively.

system, about 20% of $Fe^{2+}$ was generated in the beginning and then decreased with time (Fig. 5a). Finally, only about 5% of $Fe^{2+}$ was detected. PMS was activated by $Fe^{2+}$ within a short time and then inhibited due to the $Fe^{2+}$ poisoning. Almost all the iron species existed in the form of $Fe^{3+}$ or hydroxides precipitation, which resulted in the poor activation of PMS and unsatisfied styrene degradation. However, $Fe^{3+}$ was instantly reduced to $Fe^{2+}$ after the addition of $MoS_2$ (Fig. 5b). Nearly 90% $Fe^{2+}$ was detected in the first 5 min. The concentration of dissolved $Fe^{2+}$ fluctuated in a range of 40–60% due to a dynamic $Fe^{2+}$ regeneration and consumption. $MoS_2$ as a cocatalyst promoted the $Fe^{3+}/Fe^{2+}$ cycle, which explained the efficient activation of PMS and $O_2$ in Fenton reaction.

XPS was then applied to study the surface chemical information of $MoS_2$ powder before and after reaction (Fig. 5c and d). In the Mo3d spectrum, the fresh $MoS_2$ showed characteristic peaks at binding energy of 229.6 and 232.7 eV, corresponding to the $Mo^{4+}$ $3d_{5/2}$ and $Mo^{4+}$ $3d_{3/2}$, respectively [49]. S2p spectrums showed characteristic peaks at 162.2 and 163.2 eV, corresponding to the orbitals of $S^{2-}$ $2p_{3/2}$ and $S^{2-}$ $2p_{1/2}$. Besides, another two peaks at 235.9 and 169.0 eV were attributed to $Mo^{6+}$ and $S^{6+}$, respectively [50]. The peak located at 169.0 eV could be assigned to the $SO_4^{2-}$ species resulting from the part oxidation of $S^{2-}$ [51, 52], which was proved by the results in Fig. S14 and S15. After reaction, a slight peak displacement took place and the $Mo^{6+}$ intensity was slightly weakened. This may be caused by the dissolution of $Mo^{6+}$ from $MoS_2$ surface under weak acidic conditions and reduction of $Mo^{6+}$ to $Mo^{4+}$ through redox reactions [22,40]. The exposed $Mo^{4+}$ was further confirmed by EPR measurements and the increased pH of $MoS_2$ in solution. Under the acidic condition, the capture of protons by unsaturated S atoms on $MoS_2$ surface would be readily to form $H_2S$ (Eq. 5) [22,51]. The EPR spectrum of $MoS_2$ powder displayed a signal at $g = 2.0$, indicating the presence of sulfur vacancies (Fig. S16a). After water treatment, the signal was greatly strengthened, which confirmed the removal of S atoms. This was also confirmed by the increased pH of $MoS_2$ in solution (Fig. S16b). With the increase of washing times, the pH value of $MoS_2$ in pure water increased from acidic to nearly neutral due to the removal of $H_2S$. As a result, the oxidization of $Mo^{4+}$ to $Mo^{6+}$ on the

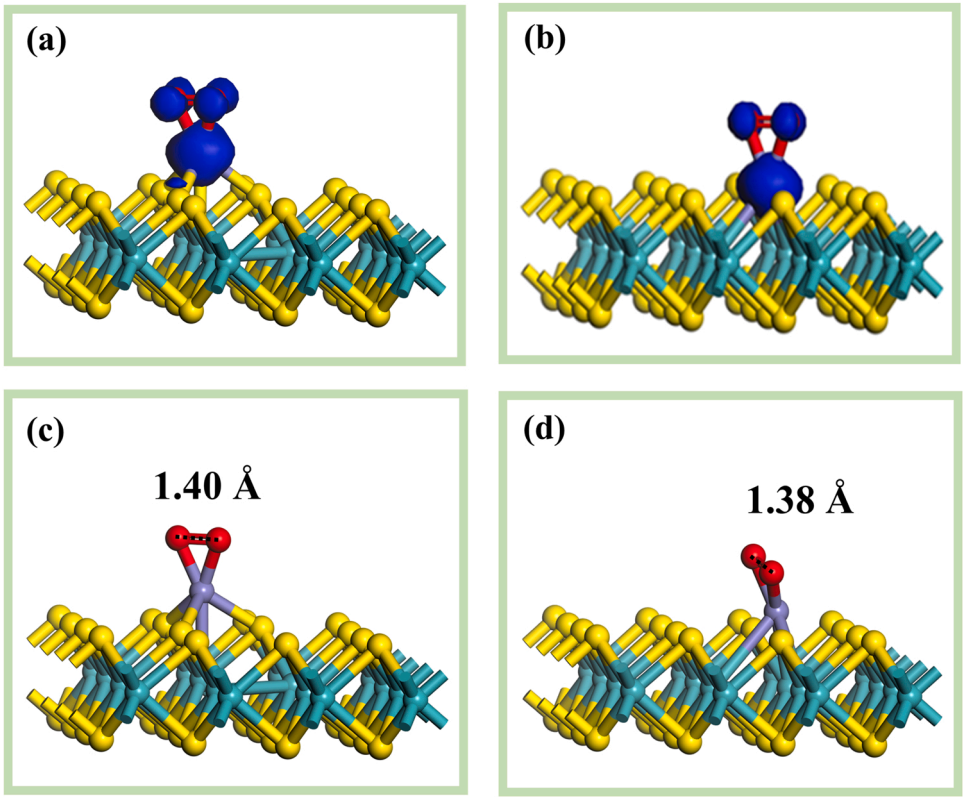


**Fig. 8.** The spin density of adsorption structure for $O_2$ on (001)-Fe-Vs (a) and (001)-Fe-G (b) surface; The adsorption of $O_2$ on (001)-Fe-G surface (c) and (001)-Fe-Vs surface (d). The indigo, yellow, purple, red and white balls represent Mo, S, Fe, O and H atoms, respectively.

surface of $MoS_2$ occurred, which was coupled with reduction of $Fe^{3+}$ to $Fe^{2+}$ (Eq. 6) [22]. The exposed $Mo^{4+}$ reacted with $Fe^{3+}$ to accelerate the regeneration of $Fe^{2+}$, which would react with PMS to generate ROS through a serious of redox reaction (Eqs. 7–11). The mechanism of the accelerated iron cycle inducing PMS and $O_2$ activation for styrene degradation in $Fe^{3+}$/PMS/$MoS_2$ system was illustrated in Fig. 6.

$$MoS_2 + 4\ H^+ \rightarrow Mo^{4+} + 2\ H_2S \quad (5)$$

$$Mo^{4+} + Fe^{3+} \rightarrow Mo^{6+} + Fe^{2+} \quad (6)$$

$$Mo^{6+} + HSO_5^- \rightarrow Mo^{4+} + SO_5^{\bullet-} + H^+ \quad (7)$$

$$Fe^{2+} + HSO_5^- \rightarrow Fe^{3+} + SO_4^{\bullet-} + OH^- \quad (8)$$

$$Fe^{2+} + HSO_5^- \rightarrow Fe^{3+} + HO^{\bullet} + SO_4^{2-} \quad (9)$$

$$Fe^{3+} + HSO_5^- \rightarrow Fe^{2+} + SO_5^{\bullet-} + H^+ \quad (10)$$

$$SO_4^{\bullet-} + OH^- \rightarrow SO_4^{2-} + HO^{\bullet} \quad (11)$$

### 3.4. ROS generation mechanism in $Fe^{3+}$/PMS/$MoS_2$ system

DFT calculation was further employed to investigate the ROS generation mechanism in $Fe^{3+}$/PMS/$MoS_2$ system. As mentioned above, the $Fe^{3+}/Fe^{2+}$ cycle in Fenton reaction [22,50] can be promoted by exposed $Mo^{4+}$ on $MoS_2$, thus its production process was first investigated (Fig. S17). The exposure of $Mo^{4+}$ on $MoS_2$ (001) surface included continuously absorbing two protons process. The heat of reaction was respectively − 0.62 and − 1.52 eV, indicating that the reaction can proceed spontaneously. Then, the $H_2S$ produced by proton absorption escaped the surface with a small energy of 0.08 eV, indicating that the sulfur atoms can easily break away from the surface to form sulfur vacancies (Vs) after the generation of $H_2S$, so as to facilitate the expose of $Mo^{4+}$.

To comprehensively investigate the activation reaction of PMS molecules in solution, five different $MoS_2$ (001) surfaces were constructed. There were original ((001)) and Vs-containing $MoS_2$ surface ((001)-Vs) (Fig. S18a and b) in the reaction solution. Based on above two types of $MoS_2$ (001) surfaces, the possible surface structures with $Fe^{2+}$ ions adsorbing were discussed. For the original configuration of $MoS_2$, $Fe^{2+}$ was most likely to be stably adsorbed on the top position of Mo atoms with an adsorption energy of − 1.95 eV ((001)-Fe) (Fig. S18c), which was stronger than that on other sites. However, for the $MoS_2$ with S vacancies, $Fe^{2+}$ may be adsorbed on the sulfur vacancies ($MoS_2$-Vs) or the position above the Mo atom near the sulfur vacancies ($MoS_2$-G). Although the adsorption energy of $Fe^{2+}$ on $MoS_2$-Vs (−4.39 eV) was stronger than that of $MoS_2$-G (−3.19 eV) (Fig. S18d and e), the energy barrier for Fe atoms to migrate between the two positions was as high as 1.88 eV. Once Fe atoms were adsorbed, they would be fixed firmly due to the strong adsorption energy. Therefore, the above five different $MoS_2$ (001) surfaces may co-exist in the solution.

In Table S1, the adsorption energies of PMS on original (001) and (001)-Vs surface (−0.53 and −1.00 eV) were weaker than that on the surface with Fe adsorbing (the $E_{ads}$ of −2.27, −2.00 and −2.01 eV for (001)-Fe, (001)-Fe-G and (001)-Fe-Vs, respectively). This indicated that the presence of $Fe^{2+}$ ion adsorbed on $MoS_2$ (001) surface can effectively promote the adsorption of PMS by $MoS_2$, which was conducive to the activation of PMS on $MoS_2$ (001) surface. The rule of electron transfer of PMS was in well accordance with the results of the adsorption energy of PMS: the stronger the $E_{ads}$ of PMS was, the more charge migrates to $Fe^{2+}$-containing surface would be. When PMS was adsorbed on the surface, the most important thing was whether it can produce radicals. Fig. 7a-b and S19 revealed that the active structure of $HO^{\bullet}$ with spin intensity only appeared on the surface of (001)-Fe-G and (001)-Fe-Vs after the dissociation of PMS. Next, the reaction to form $HO^{\bullet}$ of the adsorbed PMS was investigated by reaction energy ($\Delta E$) of PMS dissociation. In Fig. 7c

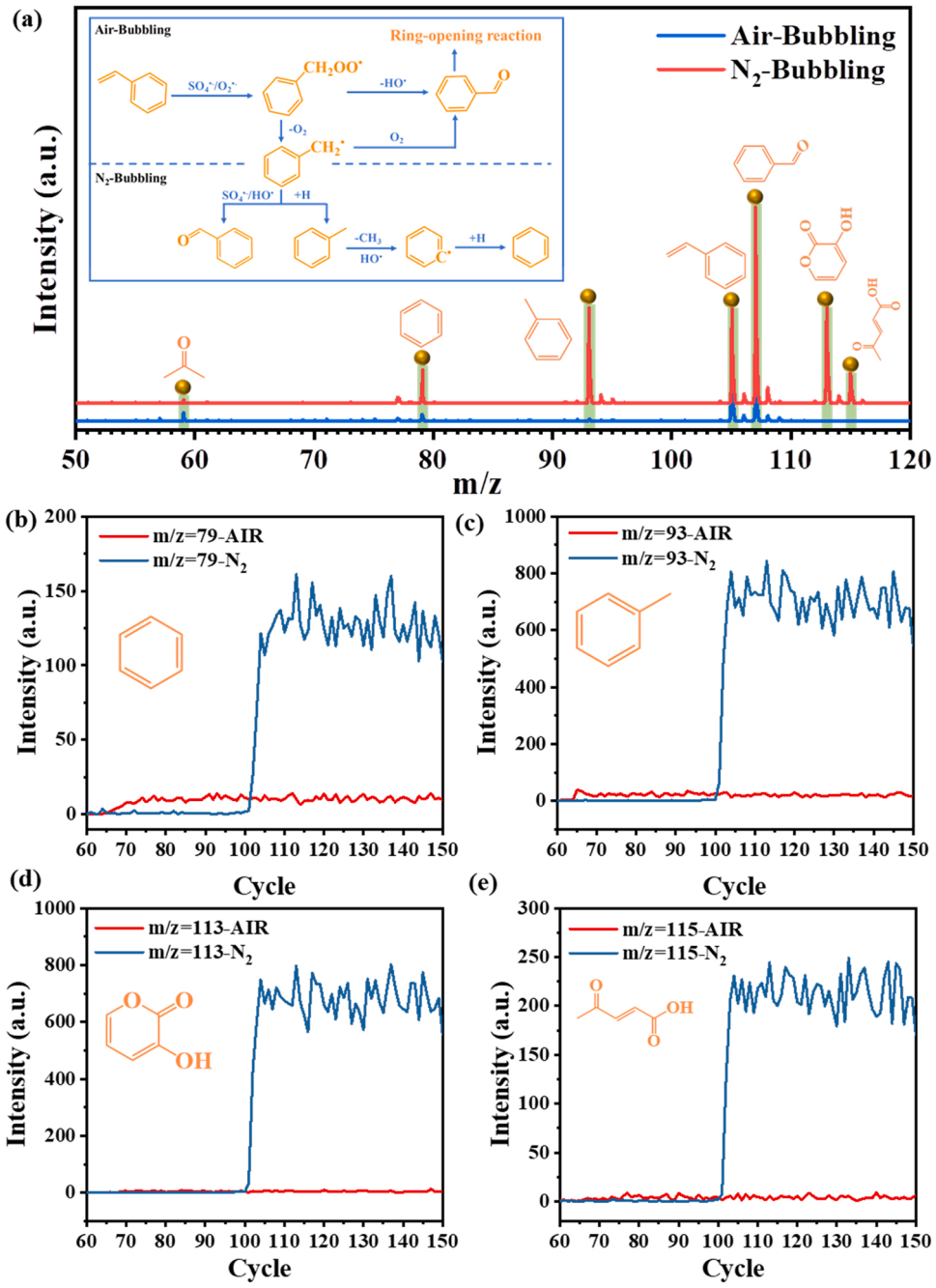


**Fig. 9.** PTR-ToF-MS spectrums of intermediates in $Fe^{3+}$/PMS/$MoS_2$ system in different conditions (a); The intensity of generated by-products in different conditions, including benzene (b), toluene (c), 3-hydroxy-2-pyranone (d) and acetylacrylic acid (e). ([Styrene]$_o$ =30 ppmv, [$Fe^{3+}$]$_o$ = 0.50 mM, [$MoS_2$]$_o$ = 15 mg, [PMS]$_o$ = 1.6 mM, pH$_o$ = 7, T = 25 ℃).

and d, the $\Delta E$ of PMS activation on (001)-Fe-G and (001)-Fe-Vs were −1.91 and −1.46 eV, indicating that this step was an exothermic reaction and occurred spontaneously at room temperature. For the adsorption structure on (001)-Fe-G surface, the O-O bond length ($l_{O\text{-}O}$) of PMS were significantly increased from 1.49 Å (free PMS molecules) to 1.68 Å, indicating that the energy reduction of the O-O bond after adsorption was beneficial to its cleavage to form radicals. While the $l_{O\text{-}O}$ of PMS on (001)-Fe-Vs was lower than that of free PMS molecules, meaning that the PMS dissociation required more energy and the reaction was difficult to proceed. Therefore, we concluded that the (001)-Fe-G surface containing $Fe^{2+}$ ion can effectively activate PMS molecules.

Simultaneously, the $Fe^{2+}$ ion on (001)-Fe-G surface can also facilitate the efficient activation of molecular $O_2$ (Fig. 8). In Table S2, the adsorption energy and charge transfer of $O_2$ on (001) surface (−0.13 eV) were weaker than that on other surface (−2.66 to −1.61 eV), meaning that $Fe^{2+}$ and Vs can promote the adsorption of $O_2$ on $MoS_2$ (001) and led to the increase of dissolved oxygen in the liquid phase. Additionally, the Mulliken charge and spin density analysis were used to determine the nature of $O_2$ on these surfaces with strong adsorption energy. The result showed that the charge transfer of $O_2$ on (001) surface was only − 0.01 e, meaning that it maintained the electrical structure of oxygen in the air and cannot be the structure of active species ($O_2^{\bullet-}$). Similarly, no spin density on the $O_2$ molecule adsorbed on (001)-Vs and (001)-Fe was observed, meaning that they were also not a radical of $O_2^{\bullet-}$ (Fig. S20). However, for the (001)-Fe-Vs and (001)-Fe-G surfaces, the spin density of adsorption structure for $O_2$ on (001)-Fe-Vs (c) and (001)-

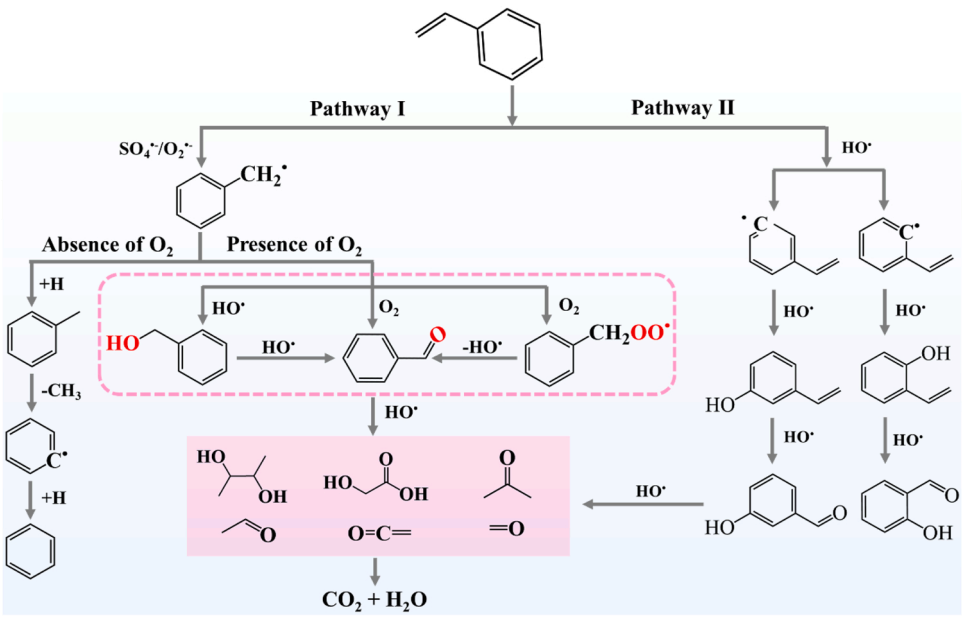


**Fig. 10.** ROS involved catalytic degradation pathway of styrene in $MoS_2$ co-catalytic $Fe^{3+}$/PMS system.

Fe-G (d) surface was obviously (Fig. 8a and b). Furthermore, the bond lengths of $O_2$ on (001)-Fe-Vs (c) and (001)-Fe-G (d) surface were changed from 1.22 Å ($O_2$ in liquid phase) to 1.38 and 1.40 Å, respectively (Fig. 8c and d). This indicated that the adsorbed $O_2$ molecule was activated and presented as the structure of $O_2^{\bullet-}$ [53]. Therefore, it was concluded that the $MoS_2$ (001) surface with $Fe^{2+}$ and Vs co-existing can effectively promote the activation of PMS and $O_2$ molecule via electron transfer in $Fe^{3+}$/PMS/$MoS_2$ system.

### 3.5. Role of molecular oxygen on styrene degradation

To further make clear the role of molecular $O_2$ on styrene degradation, the intermediates generated in $Fe^{3+}$/PMS/$MoS_2$ system were detected by PTR-ToF-MS in the presence/absence of $O_2$. As seen in Fig. 9 and Table S3 and 4, the types and concentrations of intermediates varied greatly with/without $O_2$. In the absence of $O_2$, some unsaturated hydrocarbons and benzene ring derivatives with higher toxicity were detected, including benzene (*m/z* 79), toluene (*m/z* 93), benzaldehyde (*m/z* 107), 3-hydroxy-2-pyranone (*m/z* 113) and acetylacrylic acid (*m/z* 115). The accumulation of these intermediates resulted in the unintended toxicity amplification since the benzene ring derivatives were more biotoxic than styrene. Fortunately, these benzene ring derivatives were not observed in the presence of $O_2$. The produced intermediates were mainly oxygen-containing substances with lower *m/z* values and higher water-solubility, such as formaldehyde (*m/z* 31), acetaldehyde (*m/z* 45), acetone (*m/z* 59) and acetic acid hydroxy- (*m/z* 77), implying the serious destruction of styrene chemical structure. Notably, the concentration of benzaldehyde in the $N_2$-bubbling system was much higher than that in the air-bubbling system. According to the theoretical and experimental results, it is known that $MoS_2$ as a cocatalyst greatly promoted the $Fe^{2+}$ regeneration via high-speed electron transfer process in Fenton reaction, resulting in the efficient activation of $O_2$ and PMS to form ROS including $O_2^{\bullet-}$, $HO^{\bullet}$ and $SO_4^{\bullet-}$. But the generation of radicals was greatly limited in the absence of $O_2$, which hindered the occurrence of the ring-opening reaction in a way. Thus, the aromatize intermediates would accumulate in solution, which explained the much higher concentration of benzaldehyde in the $N_2$-bubbling system. A large number of intermediates were also observed in $Fe^{3+}$/PMS system (Fig. S21 and Table S5). The rate-limiting step of $Fe^{2+}$ to $Fe^{3+}$ resulted in the poor activation of PMS and $O_2$ to form ROS, which was difficult for styrene to proceed the deep oxidation reaction after the initial degradation. Thus, the generated intermediates were accumulated in solution due to the interruption of the reaction between intermediates and ROS. Not surprisingly, the concentration and types of detected intermediates in $Fe^{3+}$/$MoS_2$ system (Fig. S22 and Table S6) were also very high and complicated. This indicated that the oxidation degradation of styrene was difficult to proceed without the attack of radicals from PMS activation.

In general, styrene was oxidized to produce styreneoxide over catalysts, which might be further oxidized to acetophenone, phenylglycol, benzaldehyde or benzoic acid [54,55]. Herein, styreneoxide or acetophenone was undetectable in $Fe^{3+}$/PMS/$MoS_2$ system. Thus, it was reasonable to believe that the degradation of styrene did not depend on epoxidation reaction. Among these intermediates, the concentration of benzaldehyde was the highest, suggesting the dominant transformation of styrene to the aldehyde. Based on the detected intermediates, the possible reaction pathways of styrene degradation were described as follows (Fig. 10): i) Direct attack of $O_2^{\bullet-}$ or $SO_4^{\bullet-}$ on styrene to form intermediate radicals through electron abstraction [44,56]; ii) Further oxygenation of the produced intermediate radicals by $HO^{\bullet}$ and $O_2$ or rearrangement to proceed ring-opening reaction; iii) Intermediates with an open-ring structure attacked by $HO^{\bullet}$ to mineralize into $CO_2$ and $H_2O$. Styrene was degraded in the presence of $O_2$, either by a vinyl side chain oxidation to phenylacetic acid followed by the aromatic ring cleavage, or by a direct attack of oxygen on the aromatic ring with its subsequent cleavage. The bond energy of C-C and C-H in aromatic ring of styrene were 5.5 and 4.8 eV, which of C-C and C-H on branch chain were 4.4 and 3.7 eV, respectively [57]. Thus, π-type C=C and σ-type C-H bonds on branched chain of styrene were more easily attacked by electrons to weaken its strong bond energy [57]. $O_2^{\bullet-}$ and $SO_4^{\bullet-}$ with much stronger oxidative selectivity directly attacked styrene molecules to produce radical cations, such as benzyl radical ($C_6H_5$-$CH_2^{\bullet}$), benzyl peroxy radical ($C_6H_5$-$CH_2OO^{\bullet}$), which would further react with $O_2$ or $HO^{\bullet}$ to form benzaldehyde (*m/z* 107), benzoic acid (*m/z* 123), phenol (*m/z* 95). Finally, the produced intermediates were decomposed by $HO^{\bullet}$ to generate low-molecular-weight organic acids or $CO_2$ and $H_2O$. However, in the absence of $O_2$, styrene was hardly attacked to form oxidation products due to the poor ROS concentration, which finally resulted in the formation of benzene ring derivatives with higher toxicity.

The above analysis proved that the $O_2^{\bullet-}$ from $O_2$ activation as well as $SO_4^{\bullet-}$ dominated the initial cleavage of terminal vinyl group on styrene to corresponding intermediate radicals, which were transformed into oxidation products by further attack of $O_2$ and $HO^{\bullet}$. In summary, the

presence of $O_2$ greatly promoted the deep oxidation of styrene and reduced by-products generation in $Fe^{3+}$/PMS/$MoS_2$ system.

## 4. Conclusion

In this work, the air-bubbling $Fe^{3+}$/PMS/$MoS_2$ system provides an efficient and stable method to activate $O_2$ for VOCs degradation in mild condition. Theoretical and experimental analysis confirm that $MoS_2$ as a cocatalyst greatly promotes $Fe^{3+}$ adsorption and $Fe^{2+}$ regeneration via high-speed electron transfer process in Fenton reaction, resulting in the efficient activation of $O_2$ and PMS to form ROS including $O_2^{\bullet-}$, $HO^{\bullet}$ and $SO_4^{\bullet-}$. The co-catalytic effect of $Fe^{3+}$/PMS/$MoS_2$ system well works for the continuous degradation of various VOCs at a broad pH range, which is favorable for practical applications. Additionally, the complete mineralization of VOCs in the presence of $O_2$ can effectively avoid secondary pollution and their environmental risks. The co-catalytic effect of $MoS_2$ in Fenton reaction achieves the efficient activation of $O_2$ and PMS through the accelerated $Fe^{3+}$/$Fe^{2+}$ cycle, which opens up a new way for VOCs waste gas treatment.

## CRediT authorship contribution statement

**Xiaowen Xie:** Conceptualization, Methodology, Data curation, Investigation, Writing – original draft, Writing – review & editing. **Jiachun Cao:** DFT theoretical calculation and analysis. **Yongjie Xiang:** Resources. **Ruijie Xie:** Resources. **Ziyi Suo:** Resources. **Zhimin Ao:** DFT theoretical calculation and analysis, Writing – review & editing, Supervision. **Xin Yang:** Supervision. **Haibao Huang:** Conceptualization, Methodology, Formal analysis, Resources, Writing – review & editing, Supervision, Project administration, Funding acquisition.

## Declaration of Competing Interest

The authors declare that they have no known competing financial interests or personal relationships that could have appeared to influence the work reported in this paper.

## Acknowledgments

This work was financially supported by the National Natural Science Foundation of China (No. 22076224, No. 22176041 and No. 21777033), Fundamental Research Funds for the Central Universities (No. 20lgjc03), Open Fund of Guangdong Province Engineering Laboratory for Air Pollution Control (No. 2019323609-01).

## Appendix A. Supporting information

Supplementary data associated with this article can be found in the online version at doi:10.1016/j.apcatb.2022.121235.

## References

[1] F.R. Dalby, S. Svane, J.J. Sigurdarson, M.K. Sorensen, M.J. Hansen, H. Karring, A. Feilberg, Synergistic tannic acid-fluoride inhibition of ammonia emissions and simultaneous reduction of methane and odor emissions from livestock waste, Environ. Sci. Technol. 54 (2020) 7639–7650.
[2] M. Ahsan, Z. Yanlin, Atmospheric volatile organic compounds (VOCs) in China: a review, Curr. Pollut. Rep. 6 (2020) 250–263.
[3] E.V. Berezina, K.B. Moiseenko, A.I. Skorokhod, N.F. Elansky, I.B. Belikov, Aromatic volatile organic compounds and their role in ground-level ozone formation in Russia, Dokl. Earth Sci. 474 (2017) 599–603.
[4] A.W. Nrgaard, V. Kofoed-Srensen, P.A. Clausen, Gd Gennaro, P. Wolkoff, Formation of ozone-initiated VOCs and secondary organic aerosol following application of a carpet deodorizer, Atmos. Environ. 222 (2020), 117149.
[5] M.S. Kamal, S.A. Razzak, M.M. Hossain, Catalytic oxidation of volatile organic compounds (VOCs)-a review, Atmos. Environ. 140 (2016) 117–134.
[6] J. Chen, X. Chen, X. Chen, W. Xu, Z. Xu, H. Jia, J. Chen, Homogeneous introduction of $CeO_y$ into $MnO_x$-based catalyst for oxidation of aromatic VOCs, Appl. Catal. B 224 (2018) 825–835.
[7] H. Huang, H. Huang, Q. Feng, G. Liu, Y. Zhan, M. Wu, H. Lu, Y. Shu, D.Y.C. Leung, Catalytic oxidation of benzene over Mn modified $TiO_2$/ZSM-5 under vacuum UV irradiation, Appl. Catal. B 203 (2017) 870–878.
[8] H. Huang, X. Ye, W. Huang, J. Chen, Y. Xu, M. Wu, Q. Shao, Z. Peng, G. Ou, J. Shi, X. Feng, Q. Feng, H. Huang, P. Hu, D.Y.C. Leung, Ozone-catalytic oxidation of gaseous benzene over $MnO_2$/ZSM-5 at ambient temperature: catalytic deactivation and its suppression, Chem. Eng. J. 264 (2015) 24–31.
[9] V.N. Lima, C.S.D. Rodrigues, R.A.C. Borges, L.M. Madeira, Gaseous and liquid effluents treatment in bubble column reactors by advanced oxidation processes: a review, Environ. Sci. Technol. 48 (2018) 949–996.
[10] C.S.D. Rodrigues, R.A.C. Borges, V.N. Lima, L.M. Madeira, p-Nitrophenol degradation by Fenton's oxidation in a bubble column reactor, J. Environ. Manag. 206 (2018) 774–785.
[11] X. Xie, R. Xie, Z. Suo, H. Huang, M. Xing, D. Lei, A highly dispersed Co-Fe bimetallic catalyst to activate peroxymonosulfate for VOCs degradation in wet scrubber, Environ. Sci. Nano 8 (2021) 2976–2987.
[12] G. Liu, J. Ji, H. Huang, R. Xie, Q. Feng, Y. Shu, Y. Zhan, R. Fang, M. He, S. Liu, X. Ye, D.Y.C. Leung, UV/$H_2O_2$: an efficient aqueous advanced oxidation process for VOCs removal, Chem. Eng. J. 324 (2017) 44–50.
[13] H. Chen, J. Liu, Y. Pei, P. Zhao, Y. Zhang, L. Yan, T. Zhang, W. Li, C. Wu, M. Hussain, Study on the synergistic effect of UV/Fenton oxidation and mass transfer enhancement with addition of activated carbon in the bubble column reactor, Chem. Eng. J. 336 (2018) 82–91.
[14] Q. Dai, K. Shen, W. Deng, Y. Cai, J. Yan, J. Wu, L. Guo, R. Liu, X. Wang, W. Zhan, HCl-tolerant $H_xPO_4$/$RuO_x$-$CeO_2$ catalysts for extremely efficient catalytic elimination of chlorinated VOCs, Environ. Sci. Technol. 55 (2021) 4007–4016.
[15] R. Xie, J. Cao, X. Xie, D. Lei, K. Guo, H. Liu, Y. Zeng, H. Huang, Mechanistic insights into complete oxidation of chlorobenzene to $CO_2$ via wet scrubber coupled with UV/PDS, Chem. Eng. J. 401 (2020), 126077.
[16] G.-D. Fang, D.D. Dionysiou, S.R. Al-Abed, D.-M. Zhou, Superoxide radical driving the activation of persulfate by magnetite nanoparticles: Implications for the degradation of PCBs, Appl. Catal. B 129 (2013) 325–332.
[17] J.Y. Kim, C. Lee, D.C. Love, D.L. Sedlak, J. Yoon, K.L. Nelson, Inactivation of MS2 coliphage by ferrous ion and zero-valent iron nanoparticles, Environ. Sci. Technol. 45 (2011) 6978–6984.
[18] Y. Mao, P. Wang, D. Zhang, Y. Xia, Y. Li, W. Zeng, S. Zhan, J.C. Crittenden, Accelerating Fe(III)-aqua complex reduction in an efficient solid-liquid-interfacial Fenton reaction over the Mn-CNH co-catalyst at near-neutral pH, Environ. Sci. Technol. 55 (2021) 13326–13334.
[19] J. Zou, J. Ma, L. Chen, X. Li, Y. Guan, P. Xie, C. Pan, Rapid acceleration of ferrous iron/peroxymonosulfate oxidation of organic pollutants by promoting Fe(III)/Fe (II) cycle with hydroxylamine, Environ. Sci. Technol. 47 (2013) 11685–11691.
[20] S. Zhou, Y. Yu, W. Zhang, X. Meng, J. Luo, L. Deng, Z. Shi, J. Crittenden, Oxidation of microcystin-LR via activation of peroxymonosulfate using ascorbic acid: kinetic modeling and toxicity assessment, Environ. Sci. Technol. 52 (2018) 4305–4312.
[21] Y. Qian, X. Guo, Y. Zhang, Y. Peng, P. Sun, C.H. Huang, J. Niu, X. Zhou, J. C. Crittenden, Perfluorooctanoic acid degradation using UV-persulfate process: modeling of the degradation and chlorate formation, Environ. Sci. Technol. 50 (2016) 772–781.
[22] M. Xing, W. Xu, C. Dong, Y. Bai, J. Zeng, Y. Zhou, J. Zhang, Y. Yin, Metal sulfides as excellent co-catalysts for $H_2O_2$ decomposition in advanced oxidation processes, Chem 4 (2018) 1359–1372.
[23] Y. Qin, F. Song, Z. Ai, P. Zhang, L. Zhang, Protocatechuic acid promoted alachlor degradation in Fe(III)/$H_2O_2$ Fenton system, Environ. Sci. Technol. 49 (2015) 7948–7956.
[24] J. Ji, R.M. Aleisa, H. Duan, J. Zhang, Y. Yin, M. Xing, Metallic active sites on $MoO_2$(110) surface to catalyze advanced oxidation processes for efficient pollutant removal, iScience 23 (2020), 100861.
[25] N. Wahba, M.F.E. Asmar, M.M.E. Sadr, Iodometric method for determination of persulfates, Anal. Chem. 31 (1959) 1870–1871.
[26] C. Liang, B. He, A titration method for determining individual oxidant concentration in the dual sodium persulfate and hydrogen peroxide oxidation system, Chemosphere 198 (2018) 297–302.
[27] Q.G. Jiang, Z.M. Ao, S. Li, Z. Wen, Density functional theory calculations on the CO catalytic oxidation on Al-embedded graphene, RSC Adv. 4 (2014) 20290–20296.
[28] J.P. Perdew, K. Burke, M. Ernzerhof, Generalized gradient approximation made simple, Phys. Rev. Lett. 77 (1996) 3865.
[29] A. Tkatchenko, M. Scheffler, Accurate molecular van der Waals interactions from ground-state electron density and free-atom reference data, Phys. Rev. Lett. 102 (2009), 073005.
[30] B. Delley, An all-electron numerical method for solving the local density functional for polyatomic molecules, J. Chem. Phys. 92 (1990) 508–517.
[31] R. Xie, D. Lei, Y. Zhan, B. Liu, C.H.A. Tsang, Y. Zeng, K. Li, D.Y.C. Leung, H. Huang, Efficient photocatalytic oxidation of gaseous toluene over F-doped $TiO_2$ in a wet scrubbing process, Chem. Eng. J. 386 (2020), 121025.
[32] A. Aziz, K.S. Kim, Synergistic effect of UV pretreated Fe-ZSM-5 catalysts for heterogeneous catalytic complete oxidation of VOC: a technology development for sustainable use, J. Hazard. Mater. 340 (2017) 351–359.
[33] P. Zhou, W. Ren, G. Nie, X. Li, X. Duan, Y. Zhang, S. Wang, Fast and long-lasting iron(III) reduction by boron toward green and accelerated Fenton chmistry, Angew. Chem. Int. Ed. 59 (2020) 16517–16526.
[34] P. Wang, X. Liu, W. Qiu, F. Wang, H. Jiang, M. Chen, W. Zhang, J. Ma, Catalytic degradation of micropollutant by peroxymonosulfate activation through Fe(III)/Fe (II) cycle confined in the nanoscale interlayer of Fe(III)-saturated montmorillonite, Water Res. 182 (2020), 116030.

[35] J. Li, Y. Wan, Y. Li, G. Yao, B. Lai, Surface Fe(III)/Fe(II) cycle promoted the degradation of atrazine by peroxymonosulfate activation in the presence of hydroxylamine, Appl. Catal. B 256 (2019), 117782.
[36] Y. Qin, F. Song, Z. Ai, P. Zhang, L. Zhang, Protocatechuic acid promoted alachlor degradation in Fe(III)/$H_2O_2$ Fenton system, Environ. Sci. Technol. 49 (2015) 7948–7956.
[37] K.Z. Huang, H. Zhang, Direct electron-transfer-based peroxymonosulfate activation by iron-doped manganese oxide (δ-$MnO_2$) and the development of galvanic oxidation processes (GOPs), Environ. Sci. Technol. 53 (2019) 12610–12620.
[38] Z. Guo, C. Li, M. Gao, X. Han, Y. Zhang, W. Zhang, W. Li, Mn-O covalency governs the intrinsic activity of Co-Mn spinel oxides for boosted peroxymonosulfate activation, Angew. Chem. Int. Ed. 60 (2021) 274–280.
[39] Q. Wang, B. Wang, Y. Ma, S. Xing, Enhanced superoxide radical production for ofloxacin removal via persulfate activation with Cu-Fe oxide, Chem. Eng. J. 354 (2018) 473–480.
[40] Q. Yi, J. Ji, B. Shen, C. Dong, J. Liu, J. Zhang, M. Xing, Singlet oxygen triggered by superoxide radicals in a molybdenum cocatalytic Fenton reaction with enhanced redox activity in the environment, Environ. Sci. Technol. 53 (2019) 9725–9733.
[41] A.M. Jones, S. Garg, D. He, A.N. Pham, T.D. Waite, Superoxide-mediated formation and charging of silver nanoparticles, Environ. Sci. Technol. 45 (2011) 1428–1434.
[42] N. Macia, R. Bresoli-Obach, S. Nonell, B. Heyne, Hybrid silver nanocubes for improved plasmon-enhanced singlet oxygen production and inactivation of bacteria, J. Am. Chem. Soc. 141 (2019) 684–692.
[43] D.R. Kearns, Physical and chemical properties of singlet molecular oxygen, Chem. Rev. 71 (1971) 395–427.
[44] J. Lee, Uv Gunten, J.-H. Kim, Persulfate-based advanced oxidation: critical assessment of opportunities and roadblocks, Environ. Sci. Technol. 54 (2020) 3064–3081.
[45] T.H. C, H.M. W., Dr. H. J. H. Fenton, F.R.S, Nature, 123 (1929) 248.
[46] M. Ren, X. Qian, M. Fang, D. Yue, Y. Zhao, Ferric (hydr)oxide/mesoporous carbon composites as Fenton-like catalysts for degradation of phenol, Res. Chem. Inter. 44 (2018) 4103–4117.
[47] Y. Mao, P. Wang, D. Zhang, Y. Xia, Y. Li, W. Zeng, S. Zhan, J.C. Crittenden, Accelerating Fe(III)-aqua complex reduction in an efficient solid-liquid-interfacial Fenton reaction over the Mn-CNH Co-catalyst at near-neutral pH, Environ. Sci. Technol. (2021).
[48] A. Georgi, M. Velasco Polo, K. Crincoli, K. Mackenzie, F.D. Kopinke, Accelerated catalytic Fenton reaction with traces of iron: an Fe-Pd-multicatalysis approach, Environ. Sci. Technol. 50 (2016) 5882–5891.
[49] Q. Yan, C. Lian, K. Huang, L. Liang, H. Yu, P. Yin, J. Zhang, M. Xing, Constructing an acidic microenvironment by $MoS_2$ in heterogeneous Fenton reaction for pollutant control, Angew. Chem. Int. Ed. Engl. (2021).
[50] L. Zhu, J. Ji, J. Liu, S. Mine, M. Matsuoka, J. Zhang, M. Xing, Designing 3D-$MoS_2$ Sponge as excellent cocatalysts in advanced oxidation processes for pollutant control, Angew. Chem. Int. Ed. 132 (2020) 14072–14080.
[51] B. Sheng, F. Yang, Y. Wang, Z. Wang, Q. Li, Y. Guo, X. Lou, J. Liu, Pivotal roles of $MoS_2$ in boosting catalytic degradation of aqueous organic pollutants by Fe(II)/PMS, Chem. Eng. J. 375 (2019), 121989.
[52] Y. Zhang, J. Niu, J. Xu, Fe(II)-promoted activation of peroxymonosulfate by molybdenum disulfide for effective degradation of acetaminophen, Chem. Eng. J. 381 (2020), 122718.
[53] W. Yang, Y. Zhu, F. You, L. Yan, Y. Ma, C. Lu, P. Gao, Q. Hao, W. Li, Insights into the surface-defect dependence of molecular oxygen activation over birnessite-type $MnO_2$, Appl. Catal. B 233 (2018) 184–193.
[54] A.M. Al-Ajlouni, J.H. Espenson, Epoxidation of styrenes by hydrogen peroxide as catalyzed by methylrhenium trioxide, J. Am. Chem. Soc. 117 (1995) 9243–9250.
[55] H. Tan, P. Kong, R. Zhang, M. Gao, M. Liu, X. Gu, W. Liu, Z. Zheng, Controllable generation of reactive oxygen species on cyano-group-modified carbon nitride for selective epoxidation of styrene, Innovation 2 (2021), 100089.
[56] J. Chen, Z. Zhang, W. Zhu, L. Zhang, B. Zhao, Y. Ji, G. Li, T. An, Superoxide radical enhanced photocatalytic performance of styrene alters its degradation mechanism and intermediate health risk on $TiO_2$/graphene surface, Environ. Res. 195 (2021), 110747.
[57] J. Zhang, J. Liu, R. Zhang, H. Hou, S. Chen, Y. Zhang, Destruction of gaseous styrene with a low-temperature plasma induced by a tubular multilayer dielectric barrier discharge, Plasma Sci. Technol. 17 (2015) 50–55.